



# The effect of temperature on injection-induced shear slip of laboratory faults in sandstone

Nao Shen<sup>1,2</sup> · Lei Wang<sup>3</sup> · Xiaochun Li<sup>2</sup>

Received: 17 May 2023 / Accepted: 18 March 2024  
© The Author(s) 2024

## Abstract

Fluid injection into subsurface reservoirs may cause existing faults/fractures to slip seismically. To study the effect of temperature on injection-induced fault slip, at a constant confining pressure of 10 MPa, we performed a series of injection-induced shear slip experiments on critically stressed sandstone samples containing saw-cut fractures (laboratory-simulated faults) under varying fluid pressurization rates (0.1 and 0.5 MPa/min, respectively) and temperatures (25, 80, and 140 °C, respectively). At 25 °C, slow fault slip events with a peak slip velocity of about 0.13 μm/s were observed on a tested sample in response to a low fluid pressurization rate of 0.1 MPa/min. In contrast, fluid injection with a high pressurization rate of 0.5 MPa/min caused fault slip events with a peak slip rate up to about 0.38 μm/s. In response to a given fluid pressurization rate, several episodes of slip events with a higher slip velocity were induced at an elevated temperature of 140 °C, indicating an appreciable weakening effect at elevated temperatures. We also experimentally constrained the rate-and-state frictional (RSF) parameters at varying effective normal stresses and temperatures by performing velocity-stepping tests. The obtained RSF parameters demonstrate that for a relatively high normal stress, increasing temperature tends to destabilize fault slip. Post-mortem microstructural observations reveal that elevated temperatures promote the generation of abundant fine-grained gouge particles associated with injection-induced shear slip. Our experiments highlight that injection-induced fault slip is affected by temperature-related wear production over the fault surface.

**Keywords** Induced seismicity · Pressurization rate · Laboratory fault (fracture) · Shear slip · Temperature

## List of symbols

$A$	Contact area	$K_m$	Loading machine stiffness
$D$	Hydraulic diffusivity	$L$	Sample length
$D_c$	Critical slip distance	$P_c, P_i,$ and	Confining pressure, injection pressure, and
$E$	Young's modulus	$P_m$	monitoring pressure, respectively
$F$	Axial force	$R$	Pressurization rate
$G$	Shear modulus	$a, b$	Friction constitutive parameters
		$d$	Diameter of a cylinder sample
		$k$	Permeability of an intact sample
		$k_c$	Critical stiffness of a fault
		$u$	Shear slip displacement
		$v$	Slip velocity
		$\nu$	Poisson's ratio
		$\eta$	Viscosity of water
		$\mu$	Friction coefficient
		$\tau$	Shear stress
		$\tau_{ss}$	Shear stress at steady state
		$\Phi$	Porosity of the intact sandstone

✉ Lei Wang  
wanglei@gfz-potsdam.de

Nao Shen  
Shenao2019@163.com

Xiaochun Li  
xcli@whrsm.ac.cn

<sup>1</sup> Changjiang Survey, Planning, Design and Research Co., Ltd, Wuhan 430010, China

<sup>2</sup> State Key Laboratory of Geomechanics and Geotechnical Engineering, Institute of Rock and Soil Mechanics, Chinese Academy of Sciences, Wuhan 430071, China

<sup>3</sup> Helmholtz Centre Potsdam, GFZ German Research Centre for Geosciences, 14473 Potsdam, Germany

## 1 Introduction

Since the seminal work of Healy et al. [26] on the Denver earthquakes, it is well established that fluid injection into subsurface reservoirs may induce earthquakes. Over the last decades, a plethora of studies have investigated induced seismicity from massive wastewater disposal, CO<sub>2</sub> sequestration, and wellbore stimulation to enhance reservoir permeability in hydrocarbon production and enhanced geothermal system (EGS) projects [2, 18, 23, 32, 37]. Previous observations indicate that induced earthquakes typically occur due to reactivating slip on pre-existing natural faults [2, 57]. Fluid injection is expected to modify stress states at faults resulting from effective normal stress changes, poroelastic stress transfer, and/or aseismic shear slip [2, 23, 24, 67]. For critically stressed fault in geothermal reservoirs, such stress changes may result in slip that may be either seismic or aseismic. However, the complexity of coupled thermo-hydrological-mechanical processes involving injected fluids and reservoir rocks poses a challenge in evaluating the stability of induced fault slip.

To unravel the physical mechanisms governing shear slip along natural faults induced by fluid injection, many experimental studies have been performed simulating injection-induced slip on faults. By increasing the injection pressure under constant normal stress and constant shear stress conditions, Nemoto et al. [42] observed that stepwise slip and shear dilation give rise to temporal fluid pressure drops on saw-cut lidate granite fractures. Using both saw-cut and tensile Sierra White granite fractures, Ye and Ghassemi [75] observed that the characteristics of shear slip induced by stepwise increasing fluid pressure depend on fracture roughness at stress relaxation condition (i.e., the constant axial piston displacement mode). Further, the spatial heterogeneity of fluid-induced slip characterized by the recorded acoustic emission hypocenter distribution in space and time is found to be correlated with fracture roughness [76]. Injection-induced slip experiments with varying fluid pressurization rates conducted on saw-cut Westerly granite samples revealed that shear slip initiation is affected by fluid pressure heterogeneity [48]. In contrast to findings from less porous and impermeable granitic rocks, injection-induced shear slip in permeable Berea and Darley Dale sandstones was found to be more sensitive to normal stress changes than to fluid pressurization [19]. The important role of rock matrix permeability in controlling the characteristics of induced slip on laboratory-sized samples has been highlighted by Rutter and Hackston [53]. Fluid injection experiments on critically stressed saw-cut samples of porous Bentheim sandstone with different pressurization rates revealed that induced shear slip mode

(steady creep vs. slow-slip events) is governed by fluid pressurization rate rather than by injection pressure [70, 71]. Injection-induced fault slip behavior was also experimentally found to be affected by the initial stress states (e.g., [14, 46]), fault surface roughness (e.g., [68, 69]), and boundary conditions (e.g., [62]). In addition to the experiments performed on bare rock surfaces, fluid injection experiments performed on samples containing carbonate-bearing fault gouge [59] and shale-rich fault gouge [58] showed that fault stability is governed by the interplay between fluid pressure and varying fault rate-and-state frictional (RSF) parameters. All aforementioned experimental studies, however, were performed at room temperature.

The stability of injection-induced fault slip relies on associated frictional properties. Some experimental studies have been conducted to examine effects of temperature on frictional behavior of simulated faults either in the absence of fluid pressure or under the constant fluid pressure. For bare rock surfaces in contact, Brace and Byerlee [10] performed triaxial compression tests on the saw-cuts and faults in dry granite and gabbro samples at a confining pressure from 100 to 500 MPa, and they found a transition from stick-slip to stable sliding as temperature was increased from 200 to 500 °C. In addition, at temperature and confining pressure less than 100 °C and 100 MPa, the triaxial experimental results of Passelègue et al. [47] suggested that increasing both temperature and confining pressure destabilizes the sliding of dry dolostone faults. This is also consistent with the sliding experiments on dry and pre-fractured granite at confining pressure of 250 MPa [64], which revealed that stick-slip is prone to occur below 300 °C, and stable sliding at higher temperature. In contrast, Lockner et al. [36] reported somewhat contradictory experimental results that the velocity dependence of friction coefficient was nearly independent of temperature (22 ~ 845 °C). The presence of pore fluids at elevated temperatures has been experimentally observed to influence the sliding behavior of faults. Velocity-stepping experiments on wet granite at hydrothermal conditions showed velocity-strengthening at room temperature but velocity-weakening from 100 to 350 °C [8, 9]. When temperature was further increased from 350 to 600 °C, there was a systematic trend from velocity-weakening to strong velocity-strengthening, which was not clearly observed on dry granite. Assuming that the mechanisms of frictional slip operating at contact points are thermally activated, the temperature dependence of friction, particularly in the presence of water, has been incorporated in a state variable constitutive relation, and the activation of several potential microscopic deformation mechanisms at varying temperatures has been discussed by Chester [15]. However, these fault reactivation and slip experiments

aforementioned were driven by a given load point displacement, rather than by fluid injection.

To date, only a limited number of laboratory experiments have been conducted to probe the fracture (fault) slip behavior induced by fluid overpressure at elevated temperatures (e.g., [4, 31]). Through injecting cold water into hot and stressed saw-cut Westerly granite fractures under drained conditions, Bauer et al. [4] observed that the combined effects of fluid pressure and cooling may cause the fracture system to deform (slip), resulting in permeability modifications. Huang et al. [28] further found that the cooling effect of fluid can cause irreversible slip on hot fracture surfaces using a 3D coupled thermo-poro-mechanical model. At a larger scale of geothermal field at Brawley, the geomechanical modeling accounting for thermo- and poroelastic stress changes associated with the geothermal operations revealed that pore pressure changed and thermal unclamping (cooling effects) drove aseismic motion on a normal fault intersecting the geothermal reservoir [29]. Kc and Ghazanfari [31] experimentally found that fault slip induced by fluid pressure gradients resulted in permeability enhancement likely due to self-propping of asperities. The triaxial shear-flow experiments performed by Ji et al. [30] suggested that an elevated temperature favors a more uniform fluid pressure distribution over the fault surface by reducing water viscosity.

In this study, we present results of laboratory fluid injection experiments performed at varying temperature and pressurization rate conditions on critically stressed sandstone samples containing saw-cut faults. We experimentally determined the RSF parameters of water-saturated fractured samples at varying pressures and temperatures using velocity-stepping tests. We studied the characteristics of injection-induced shear slip at varying temperatures and analyzed the post-mortem microstructures.

## 2 Materials and methods

### 2.1 Rock sample preparation

Sandstone samples used in this study are from Sichuan Province, China. This sandstone is composed of 50.73% quartz, 34.01% albite, 10.59% calcite, 3.32% illite, and 1.36% montmorillonite, respectively. The average grain size is about 0.1 mm. Samples were prepared as cylinders with dimensions of 50 mm in diameter ( $d$ ) and 100 mm in length ( $L$ ) (Fig. 1). Uniaxial compression tests were performed to determine Young's modulus ( $E \approx 6.1$  GPa), Poisson's ratio ( $\nu \approx 0.16$ ), and uniaxial compressive strength ( $\approx 46$  MPa). Porosity of the sandstone was determined to be about 10%.

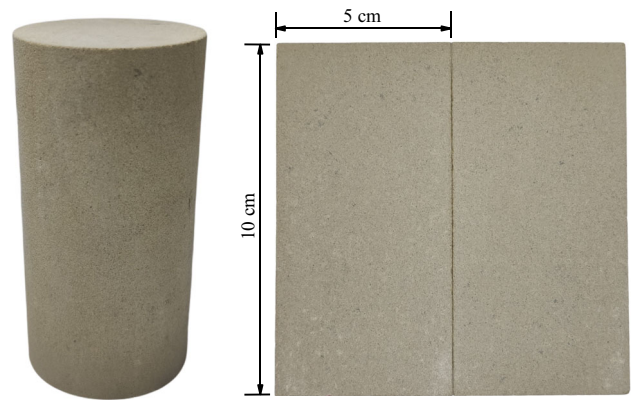


**Fig. 1** Photographs of intact cylindrical and saw-cut sandstone samples

The cylindrical samples were split into two equal halves along the sample axis using the automatic wire cutting machine, and then the surfaces were polished using the 1000#-grit silicon carbide abrasive paper. We prepared five saw-cut samples (samples SC1–SC5), whose surfaces were scanned using a 3D optical profilometer with a pixel width of 50  $\mu\text{m}$  before experiments. Here, we used the root mean square roughness,  $h_{\text{rms}}$ , to evaluate the ensemble roughness characteristics of 2D sample surfaces. The values of  $h_{\text{rms}}$  for these saw-cut surfaces were measured to be 6 ~ 15  $\mu\text{m}$ . Following Barton [3], the joint roughness coefficient (JRC) was calculated to be negative, suggesting that the saw-cut surfaces were very flat.

Using the pulse decay method, we measured the permeability of intact samples, which is about  $1.36 \times 10^{-19} \text{ m}^2$  at an effective confining pressure of 6 MPa. The low permeability of the rock matrix results in a sufficiently long diffusion time for pore pressure equilibrium within rock matrix (see Appendix 1). Thus, we assume that fluid pressurization mainly affects the high-permeability fracture interface separating the two low-permeability wall rocks, as confirmed by minimal observed delay of fluid pressure between the two ends of samples during fluid injection (see Sect. 3.1).

### 2.2 Experimental setup and experimental procedures

Our laboratory experiments were carried out using a triaxial direct-shear apparatus [77], which consists of a servo-controlled axial loading unit (loading capacity of 250 kN), closed-loop controlled confining pressure (maximum of 70 MPa using silicone oil as the pressure medium), fluid pressure (maximum of 40 MPa) units (ISCO pumps), a temperature control unit (room temperature to 150  $^{\circ}\text{C}$ ), and a data acquisition system. The stiffness of machine plus

assembly is about 35.65 MPa/mm. The fractured sample and L-shaped shear module were encapsulated in a Teflon heat-shrink tube (from Penn & Nitto Corp., Japan), which was used to isolate the sample from the silicone oil (Fig. 2). Two internal linear variable displacement transducers (LVDTs) with resolution of  $\pm 0.1 \mu\text{m}$  were used to measure the load point displacement. Here, the mean value obtained by LVDTs is considered as the shear slip displacement ( $u$ ) along the fault, ignoring the elastic deformation of the rock matrix caused by minor changes of stress state. We then updated the contact area ( $A$ ) of fault zone associated with the recorded shear slip data. The axial force ( $F$ ) loaded on the tested samples was measured using an internal load cell (resolution of  $\pm 0.001 \text{ kN}$ , from GDS, Hampshire, UK). The resistance of compliant silicone plugs is negligible. Thus, the shear stress ( $\tau$ ) can be directly calculated by  $\tau = F/A$ . The fault-normal deformation was measured by two extensometers (resolution of  $\pm 1 \mu\text{m}$ ) located at about 3 cm distance from each end of the sample (Fig. 2a). The extensometers clamp the cylinder at two opposite points with their connection normal to the fault plane. Fluid pressure changes at two ends of fractured samples (i.e., injection pressure  $P_i$  and monitoring pressure  $P_m$ ) were monitored by two fluid pressure transducers (resolution of  $\pm 0.01 \text{ MPa}$ ) installed at fluid inlet and outlet, respectively (Fig. 2a). The temperature inside the pressure chamber was controlled by four internal heaters (Fig. 2b) with an accuracy of  $\pm 0.5 \text{ }^\circ\text{C}$ . There is a thermocouple mounted inside the pressure vessel, measuring real-time temperature changes. The more details about the experimental apparatus can be found in Zhang et al. [77] and Shen et al. [61]. Throughout the experiments, all

experimental data were recorded at a sampling rate of 10 Hz.

### 2.2.1 Injection-induced shear slip tests

The triaxial cell was filled with silicone oil after the sample assembly was installed (Fig. 2b). Prior to testing, the sample was first heated to the target temperature, followed by increasing confining pressure ( $P_c$ ) to a target value of 10 MPa. To reach a steady state, the tested sample was kept at constant temperature and constant confining pressure for two hours. Subsequently, the sample was placed under a vacuum for about 1 h and then saturated with deionized water at 2-MPa fluid pressure. Then all tests were performed in the following three consecutive stages. First, the axial force was progressively increased at a constant displacement rate of 0.3 mm/min up to peak shear stress (i.e., Stage 1 in Fig. 3). Subsequently, the axial piston was stopped, and axial stress was allowed to relax and settle at a steady-state value ( $\tau_{ss}$ ). Then the shear stress was adjusted to about  $0.92\tau_{ss}$  by retracting the axial piston slowly (i.e., Stage 2 in Fig. 3). From this point on, the axial piston position was fixed throughout the subsequent fluid injection test, following the method proposed by Ye and Ghassemi [75]. The fluid (water) was directly pumped into the fault from the bottom (upstream), while the top end of the sample (downstream) was undrained. Injection pressure ( $P_i$ ) was increased in a stepwise manner from 2 to 6 MPa at a rate of 0.1 MPa/min (i.e., Stage 3 in Fig. 3a) or 0.5 MPa/min (i.e., Stage 3 in Fig. 3b), consisting of four consecutive fluid injection periods. During each fluid injection period, fluid pressure was increased by 1 MPa over a time period

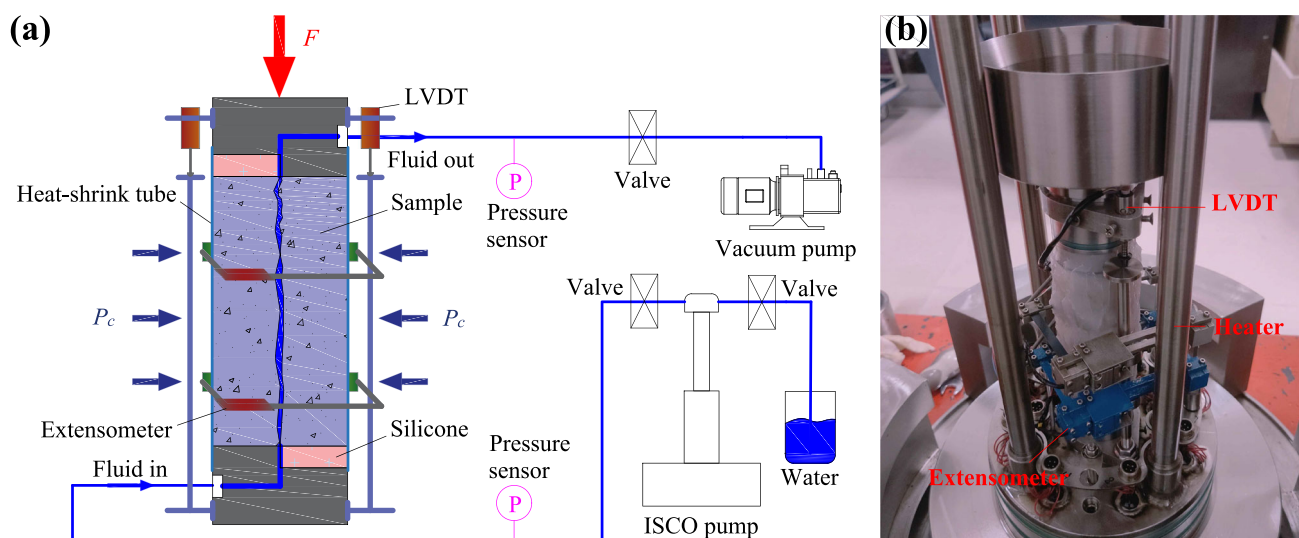


**Fig. 2** a A schematic diagram of the experimental apparatus. b Photograph of the mounted sample assembly

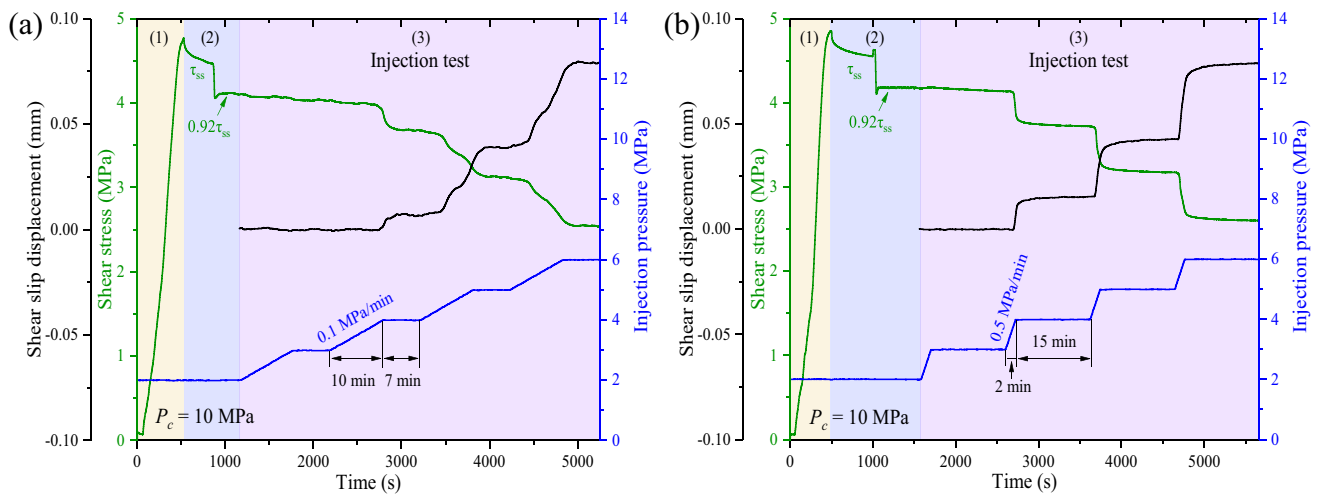


**Fig. 3** Shear slip displacement (black), shear stress (green), and injection pressure (blue) as a function of time throughout the whole experiment at pressurization rates of 0.1 MPa/min (a) and 0.5 MPa/min (b), respectively. The whole experiment is composed of three consecutive stages, as indicated by three different color-shaded areas. Note that the shear slip displacement is set to zero at the beginning of the third stage for better comparison among all experiments (color figure online)

of 10 min for a pressurization rate of 0.1 MPa/min or 2 min for a pressurization rate of 0.5 MPa/min, and then the fluid pressure was maintained constant for 7 or 15 min (Fig. 3), respectively. Table 1 lists the main parameters obtained in the injection-induced shear slip tests.

After each experiment, the fault surface was scanned again using the 3D laser scanner. In addition, the microstructures of the fault surface and gouge production were analyzed using a scanning electron microscope (SEM, Tescan Mira3 Zeiss Sigma 500).

### 2.2.2 Velocity-stepping tests

The single degree-of-freedom spring-slider model with the RSF constitutive law is commonly used to describe the frictional behavior of a fault [17, 52], as expressed by

$$\mu = \mu_0 + a \ln\left(\frac{v}{v_0}\right) + b \ln\left(\frac{\theta v_0}{D_c}\right) \quad (1)$$

where  $\mu$  is the friction coefficient;  $\mu_0$  is the reference friction at a reference slip velocity  $v_0$ ;  $a$  and  $b$  represent the direct and evolution effects for the friction coefficient reaching a new steady state over a critical slip distance  $D_c$  (Fig. 4) as slip velocity is stepped from  $v_0$  to  $v$ ; and  $\theta$  is the state variable. Using the slip law [17, 52], the evolution of state variable  $\theta$  with time  $t$  is given by

$$\frac{d\theta}{dt} = -\frac{v\theta}{D_c} \ln\left(\frac{v\theta}{D_c}\right) \quad (2)$$

For steady-state friction, the state variable remains unchanged over time (i.e.,  $d\theta/dt = 0$  holds). Thus, the frictional stability parameter ( $a-b$ ) at steady state can be obtained from Eq. (1), as given by

**Table 1** Summary of experimental conditions and results of injection-induced shear slip tests

Samples	$P_c$ (MPa)	$P_i$ (MPa)	$R$ (MPa/min)	$T$ (°C)	$0.92\tau_{ss}$ (MPa)	$\mu$	$\Delta\tau$ (MPa)	$\Delta V_f$ (mL)	$\Delta u$ ( $\mu\text{m}$ )	$v_{\text{peak}}$ ( $\mu\text{m/s}$ )
SC1	10	2–6	0.1	25	4.68	0.58–0.75	1.73	1.08	87.3	0.13
SC2	10	2–6	0.1	80	4.10	0.51–0.66	1.57	1.24	79.7	0.12
SC3	10	2–6	0.1	140	4.17	0.52–0.67	1.62	1.73	78.9	0.28
SC4	10	2–6	0.5	25	4.17	0.52–0.69	1.57	1.36	78.6	0.38
SC5	10	2–6	0.5	140	4.29	0.53–0.71	1.75	1.22	92.8	0.58

$P_c$  is the confining pressure,  $P_i$  is the fluid pressure,  $R$  is the fluid pressurization rate,  $T$  is the temperature,  $0.92\tau_{ss}$  is the initial shear stress of the fractured sample before fluid injection,  $\mu$  is the range of friction coefficient during fluid injection,  $\Delta\tau$  is the shear stress drop associated with injection-induced slip,  $\Delta V_f$  is the total injected fluid volume,  $\Delta u$  is the injection-induced total slip displacement, and  $v_{\text{peak}}$  is the peak slip velocity

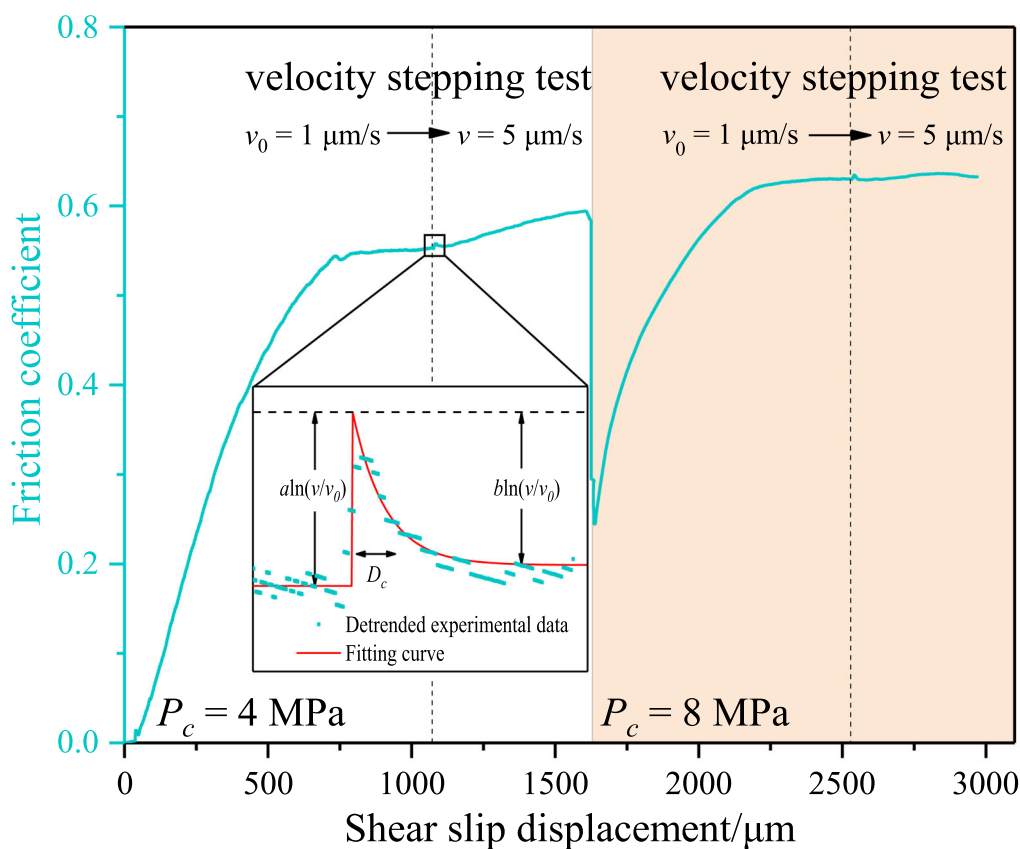


**Fig. 4** A typical experimental curve (i.e., friction coefficient vs. shear slip displacement) for velocity-stepping tests at confining pressures of 4 and 8 MPa, respectively (i.e., Test #3 and Test #4, respectively, see Table 2). When shear velocity is stepped from 1 to 5  $\mu\text{m/s}$  (enlarged in the black rectangle), the RSF parameters ( $a$ ,  $b$ , and  $D_c$ ) can be estimated from the experimental friction data with linear least squares regression

**Table 2** Summary of experimental conditions and results of velocity-stepping tests

Test numbers	$P_c$ (MPa)	$T$ ( $^{\circ}\text{C}$ )	$\mu_0$	Trend	Comment
Test #1	4	25	0.656	Velocity-strengthening	Water-saturated
Test #2	8	25	0.655	Velocity-neutral	Water-saturated
Test #3	4	80	0.553	Velocity-strengthening	Water-saturated
Test #4	8	80	0.630	Velocity-neutral	Water-saturated
Test #5	4	140	0.559	Velocity-strengthening	Water-saturated
Test #6	8	140	0.631	Velocity-weakening	Water-saturated

$P_c$  is the confining pressure,  $T$  is the temperature, and  $\mu_0$  is the reference steady-state friction coefficient at slip velocity of 1  $\mu\text{m/s}$

$$a - b = \frac{\mu - \mu_0}{\ln(v/v_0)} \quad (3)$$

A positive value of  $(a-b)$  indicates that the friction coefficient increases with increasing slip velocity (i.e., velocity-strengthening behavior, promoting stable slip), whereas a negative value of  $(a-b)$  represents velocity-weakening behavior, and slip may be unstable once the critical stiffness is met.

We obtained the frictional constitutive parameters (i.e.,  $a$ ,  $b$ , and  $D_c$ ) by performing velocity-stepping tests on

water-saturated saw-cut sandstone samples at varying normal stress and temperature conditions (Table 2). Before testing, the sample temperature was elevated to the target value and kept constant for 2 h. Then, the sample was saturated with deionized water of 0.1 MPa under a given confining pressure (4 and 8 MPa in this study). To avoid potential local fluid pressure heterogeneity associated with shear-enhanced dilation or compaction [35, 62] during shear slip, the fluid overpressure of 0.1 MPa applied for saturation was removed before subsequent shearing. Note

that the selected confining pressure values (i.e., 4 and 8 MPa in this study) represented the lower and upper bounds of evolving effective normal stress at which the induced slip occurred in the fluid injection experiments. After reaching a relatively steady shear strength, a velocity-stepping test was carried out by varying slip velocity from 1 to 5  $\mu\text{m/s}$  (Fig. 4). We ignored the effect of fault surface wear at a low confining pressure of 4 MPa on the subsequent velocity-stepping tests performed at a higher confining pressure of 8 MPa. Two velocity-stepping tests were performed on the same sample at a given temperature (Fig. 4).

### 2.2.3 Data processing

In our experiments, axial piston displacement was measured with an external grating ruler. In addition, the shear slip displacement was recorded by two internal LVDTs, i.e., the mean value was used in this study. The readout of a LVDT may be influenced by environmental temperature change due to the thermal deformation of built-in metallic parts and the temperature dependence of electro-magnetic properties of iron core and coil [40, 74]. Thus, we carefully calibrated the measured shear slip displacement by considering the temperature variation in the pressure vessel. Further, we obtained slip velocity from the time derivative of the corrected shear slip displacement. As mentioned before, we also deployed two extensometers located at 3-cm distance to each end of the sample to monitor fault-normal deformation (negative for dilation). We found the two extensometers' measurements consistent throughout all the experiments, indicating that the fault-normal deformation was fairly similar across the sample. Hence, the corresponding mean value was used to represent fault-normal deformation.

The density of water varies at different temperatures, from 999.0  $\text{kg/m}^3$  at 25  $^\circ\text{C}$ , 973.5  $\text{kg/m}^3$  at 80  $^\circ\text{C}$  to 928.0  $\text{kg/m}^3$  at 140  $^\circ\text{C}$ , respectively (<https://webbook.nist.gov/chemistry/>). In this study, the real water volume injected into the fault zone at high temperatures was obtained by multiplying the water density ratio (the ratio of water density at room temperature to that at high temperatures) with the fluid volume change recorded by the ISCO pump at room temperature (25  $^\circ\text{C}$ ). During the period of fluid injection-induced shear slip (i.e., Stage 3 in Fig. 3a), a total water volume less than 1.5 mL was injected into the laboratory fault within 68 min. Hence, it is reasonable to assume that the heat exchange between injected cool water and hot fractured sandstone sample (e.g., the sample SC3 in Table 1) was completed shortly after the commencement of fluid injection. This suggests that the potential cooling effect of fluid injection on induced fault slip behavior in this study may be negligible.

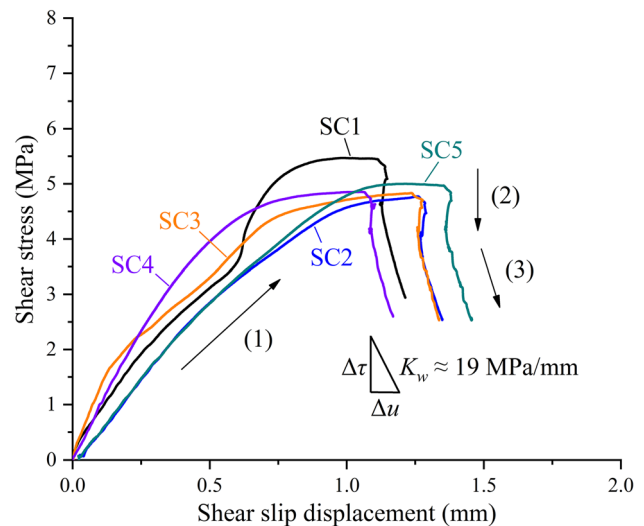


**Fig. 5** Evolution of shear stress with shear slip on faults. The numbers in brackets correspond to the three stages showed in Fig. 3. The decay curve of shear stress against slip displacement beyond fault reactivation in Stage 3 may give the slip-weakening rate (unloading stiffness)  $K_w$ , which is about 19 MPa/mm for all tested faults

Based on the experimental results of velocity-stepping tests, the inversion for RSF parameters ( $a$ ,  $b$ , and  $D_c$ ) was achieved using the software package developed by Skarbek and Savage [63] based on linear least squares regression.

## 3 Experimental results

### 3.1 Characteristics of injection-induced shear slip

We performed injection-induced shear slip experiments on critically stressed samples with saw-cut faults (Table 1). Except for the observed slight delay between injection pressure  $P_i$  and monitoring pressure  $P_m$  during fluid overpressure in samples SC2 and SC5, the fluid pressure was found to be homogeneously distributed across the whole fault surfaces.

During initial loading of all samples (Stage 1), we observed an almost linear increase in shear stress until corresponding peak strength was reached (see Fig. 5). Beyond peak strength, the loading piston was fixed, and shear stress gradually relaxed to a steady-state value  $\tau_{ss}$  (i.e., 4.5 ~ 5.1 MPa). Then, we reduced the shear stress to about  $0.92\tau_{ss}$  by slowly retracting the loading piston (i.e., Stage 2 in Figs. 3 and 5). This guaranteed that all faults were critically stressed prior to fluid injection. During fluid injection, all faults first remained locked. Once slip was initiated, shear stress dropped gradually (i.e., Stage 3 in Figs. 3 and 5). As shown in Fig. 5, using the linear regression method, the values of weakening rate ( $K_w \approx \Delta\tau/\Delta u$ ) of all tested samples were approximately 19 MPa/mm.

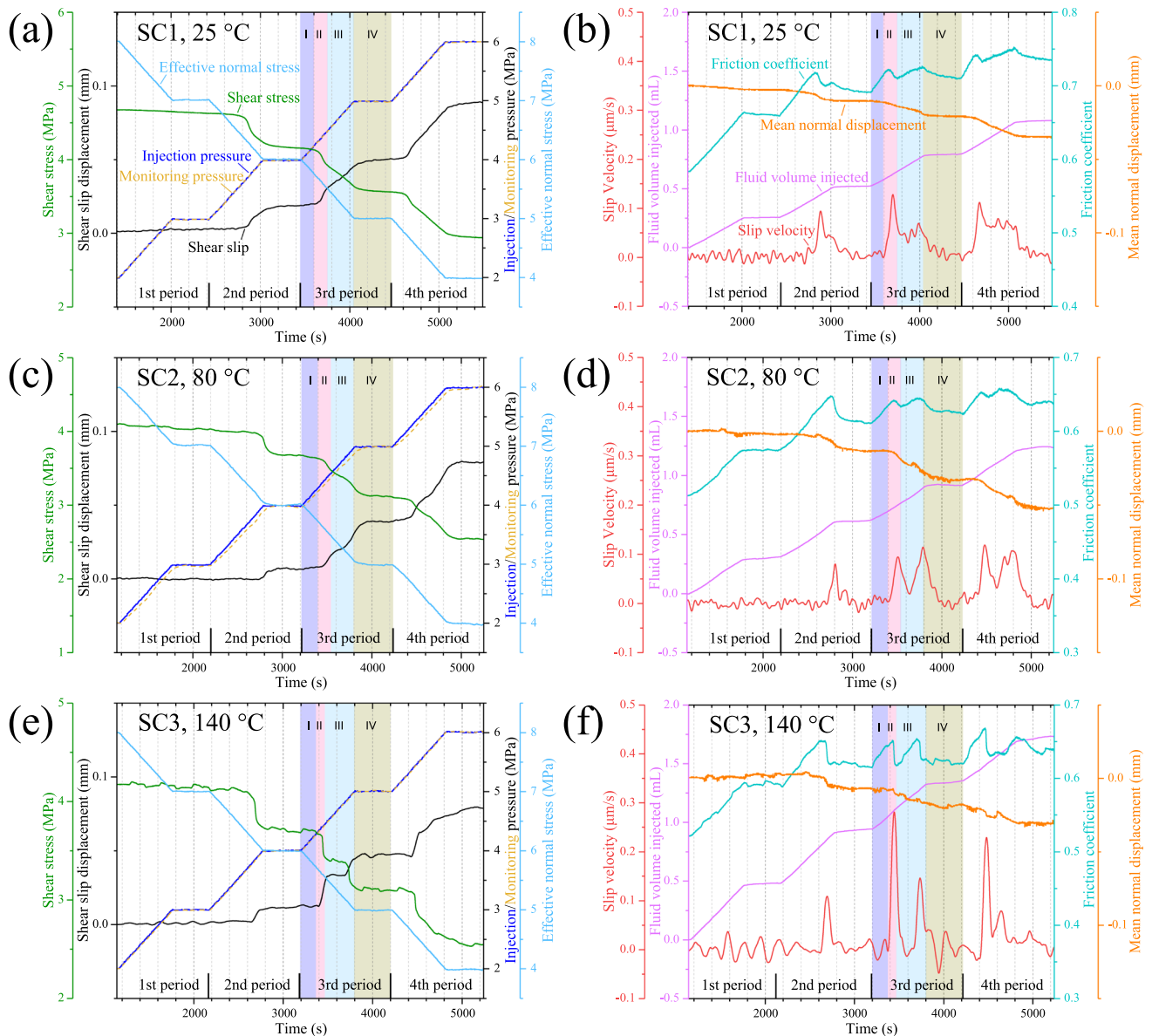


**Fig. 6** Time history of shear stress, shear slip displacement, injection pressure, monitoring pressure (dashed line), effective normal stress, slip velocity, fluid volume injected, friction coefficient, and normal displacement (negative for dilation) since fluid injection at a pressurization rate of 0.1 MPa/min on faults (i.e., Stage 3 in Fig. 3). **a, b** Sample SC1 at temperature of 25 °C; **c, d** Sample SC2 at temperature of 80 °C; and **e, f** Sample SC3 at temperature of 140 °C. The whole fluid injection process can be divided into four periods, and the representative third injection period is divided into four (i.e., I, II, III, and IV) phases

The instantaneous sample-averaged friction coefficient ( $\mu$ ) may be estimated by  $\mu = \tau / (P_c - P_f)$  with  $(P_c - P_f)$  representing effective normal stress and  $P_f$  representing the mean value of injection pressure and monitoring pressure. The friction coefficient of all tested samples varied between 0.6 and 1.0 (Table 1) after shear stress started to drop. In the following, we describe the injection-induced slip behavior of tested samples during Stage 3 in more detail.

After injection started (i.e.,  $P_i$  was increased from 2 to 3 MPa with a rate of 0.1 MPa/min), faults in all samples remained locked initially (Fig. 6a, c, e). However, for

faults deformed at elevated temperatures, we observed a minor decline in shear stress, which would be discussed in Sect. 5.2. Friction coefficient showed a progressive growth as fluid pressure increased (Fig. 6b, d, f). Meanwhile, only a small amount of fault-normal dilation was observed for faults at different temperatures (Fig. 6b, d, f).

During the second injection period (i.e.,  $P_i$  was increased from 3 to 4 MPa), samples SC1, SC2, and SC3 approached failure, and shear slip started. The onset of shear slip in response to fluid injection was accompanied by a significant shear stress drop and fault-normal dilation.



Specifically, slip initiation occurred at fluid pressures of about 3.47, 3.88, and 3.75 MPa for samples SC1, SC2, and SC3, respectively (Fig. 6a, c, e). As shown in Fig. 6b, d, f, a slow fault slip event was observed with a peak slip velocity of about 0.1  $\mu\text{m/s}$ , which was accompanied by a sudden decrease in friction coefficient. Moreover, the decay rates of friction coefficient showed a growing trend, resulting from a faster shear stress drop.

For each individual fault, we found that slip characteristics were similar for the third and the fourth fluid injection periods. To clearly describe the dynamics of induced slip by fluid injection, we divided the third fluid injection period into four phases (Fig. 6). After fluid injection started, all faults remained locked until the onset of slip occurred (Phase I in Fig. 6a, c, e). As fluid pressure increased continuously, slip accelerated to peak velocity (0.13, 0.09, and 0.28  $\mu\text{m/s}$  for SC1, SC2, and SC3, respectively) and decelerated, accompanied by a rapid drop in shear stress and shear-enhanced dilation (Phase II in Fig. 6b, d, f). A gradual decrease in friction coefficient was observed concurrently. In the following third phase, slip behavior of faults varied depending on temperature. Sample SC1 loaded at room temperature underwent a long-

lasting relaxation phase at constant slip rate (steady slip) of about 0.05  $\mu\text{m/s}$  until the shut-in of fluid injection, and the friction coefficient increased slowly with shear slip. This slip behavior was similar to observations of Wang et al. [71] on saw-cut Bentheim sandstone in response to step-wise fluid injection. In contrast, at 80 and 140  $^{\circ}\text{C}$ , the second slow fault slip event with peak velocities of 0.1  $\mu\text{m/s}$  and 0.15  $\mu\text{m/s}$  was observed on samples SC2 and SC3, respectively, toward the end of fluid pressurization (see Phase III in Fig. 6d, f). Such slow fault slip events were accompanied by a rapid reduction in friction coefficient, especially at 140  $^{\circ}\text{C}$ . The distinct slip responses at similar injection conditions between samples SC1, SC2, and SC3 highlight that slip behavior on faults depends on temperature. For all tests, slip decelerated, and faults became locked after fluid pressurization ceased (see Phase IV in Fig. 6b, d, f). This was also accompanied by a gradual decrease in friction coefficient.

We increased the fluid pressurization rate to 0.5 MPa/min on samples SC4 and SC5 (Fig. 7). The time duration of each injection period (composed of fluid pressurization and pressure plateau substages) lasted for 17 min, as the samples SC1–SC3 did. These two samples started to slip

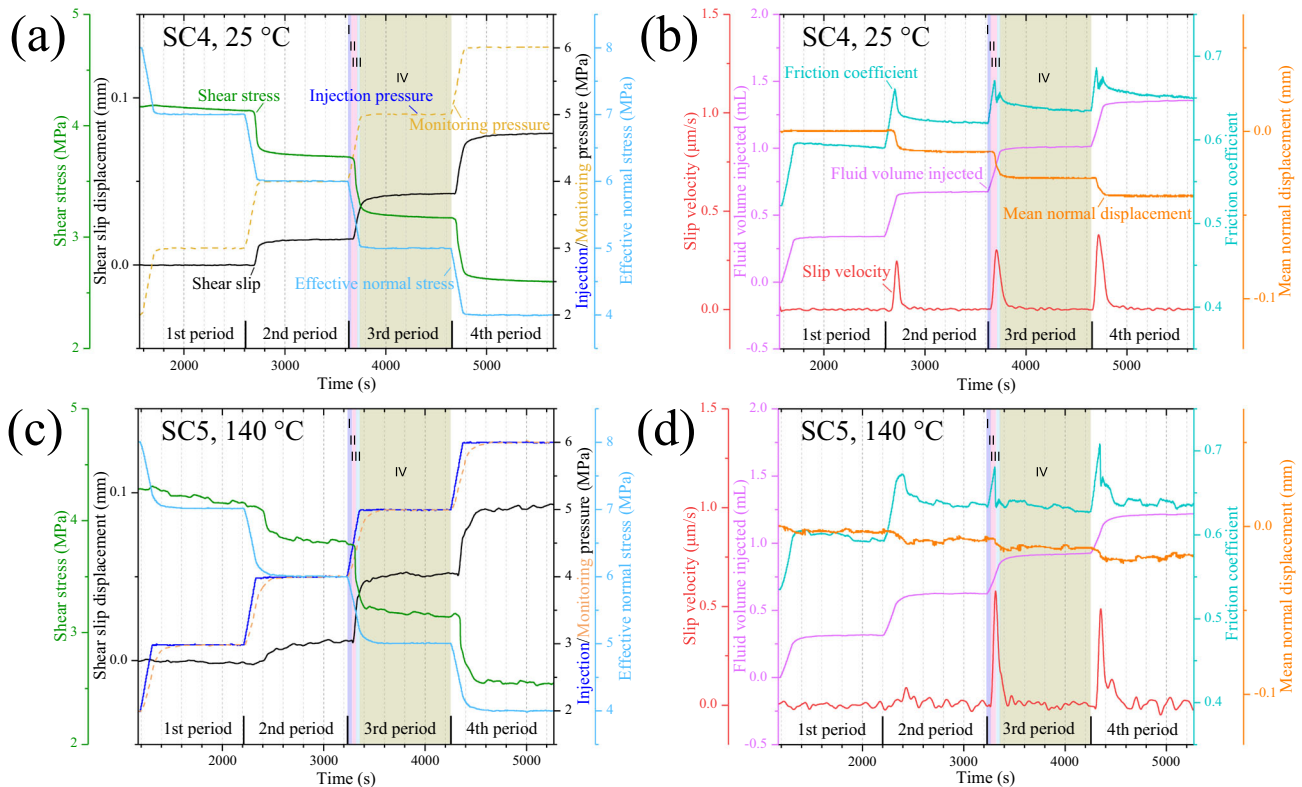


**Fig. 7** Time history of shear stress, shear slip displacement, injection pressure, monitoring pressure (dashed line), effective normal stress, slip velocity, fluid volume injected, friction coefficient, and normal displacement (negative for dilation) since fluid injection at a pressurization rate of 0.5 MPa/min on faults (i.e., Stage 3 in Fig. 3). **a, b** Sample SC4 at a temperature of 25  $^{\circ}\text{C}$  and **c, d** Sample SC5 at a temperature of 140  $^{\circ}\text{C}$ . The whole fluid injection process can be divided into four periods, and the representative third injection period is divided into four (i.e., I, II, III, and IV) phases

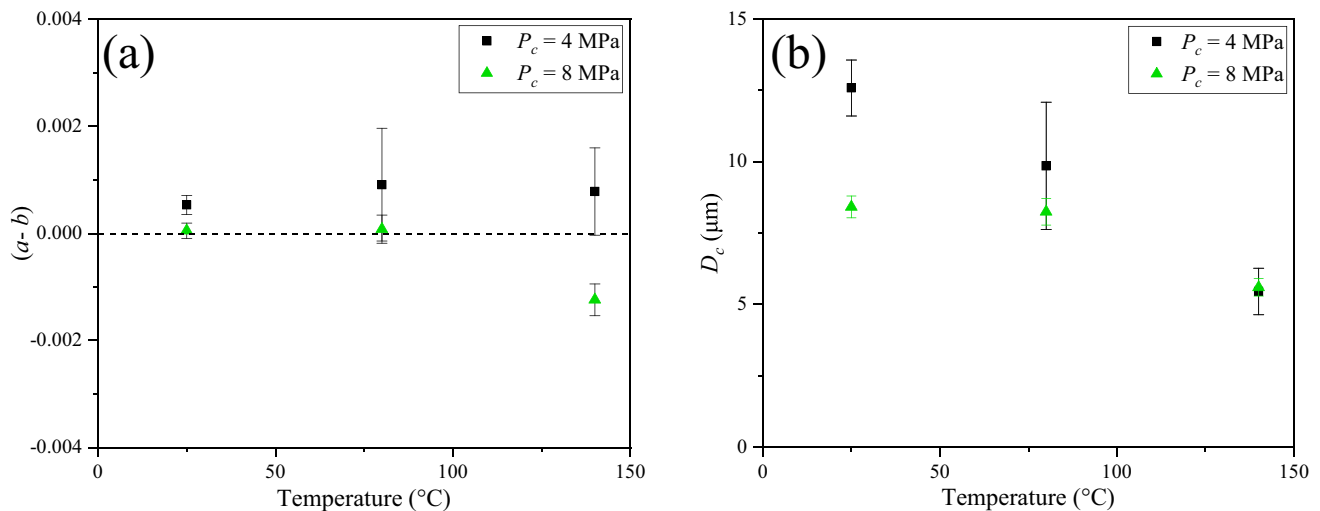


**Fig. 8** RSF parameters ( $a$ ,  $b$ , and  $D_c$ ) estimated from the inversion of experimental data of velocity-stepping tests. **a** Evolution of frictional stability parameter ( $a-b$ ) as a function of temperature at different confining pressures. **b** The characteristic slip distance  $D_c$  as a function of temperature at different confining pressures. Error bars represent standard deviation

during the second injection period, but sample SC4 produced a relatively larger slip rate. In response to the higher injection power, the sample SC4 at room temperature achieved a peak slip velocity of around  $0.24 \sim 0.38 \mu\text{m/s}$  (Fig. 7b). During the third and the fourth injection periods, the friction coefficient of the sample SC4 dropped sharply in Phase II and recovered slightly afterward. The sample SC5 showed a relatively low permeability compared to the sample SC4, with a slight fluid pressure difference between two sample ends during fluid pressurization. Subjected to a higher pressurization rate compared to sample SC3, the elevated temperature of  $140^\circ\text{C}$  enhanced the peak slip velocity on fault (up to  $\sim 0.58 \mu\text{m/s}$ ) (Fig. 7d). Similar to the sample SC3, the friction coefficient of the sample SC5 dropped quickly when it approached the peak slip velocity, and subsequently there was no apparent restrengthening trend.

### 3.2 RSF parameters at varying pressures and temperatures

The evolution of RSF parameters at varying pressures and temperatures was experimentally estimated on saw-cut sandstone samples under water-saturated conditions. At a confining pressure of 4 MPa, all samples displayed velocity-strengthening behavior with a positive frictional parameter ( $a-b$ ), regardless of temperature changes (Fig. 8a). In contrast, a transition from velocity-neutral to velocity-weakening with increasing temperature was observed at a higher confining pressure of 8 MPa (Fig. 8a). Our results also showed that the characteristic slip distance ( $D_c$ ) decreased with temperature (Fig. 8b). The magnitude of  $D_c$  ranged from  $5.5$  to  $12.6 \mu\text{m}$  at confining pressure of 4

MPa and from  $5.6$  to  $8.4 \mu\text{m}$  at confining pressure of 8 MPa, respectively (Fig. 8b).

## 4 Microstructural observations

After the experiments, we clearly observed the fault gouge production associated with shear slip that was distributed over the fault surfaces. As shown in Fig. 9, the microstructural characterization of fault surfaces was performed using scanning electron microscope (SEM) before and after testing. For the sample surface before injection test (Fig. 9a), one layer of cemented grains on the bare surface was partially crushed during the sample preparation, and boundaries between grains can be faintly visible. By contrast, micrographs of deformed samples after tests at different temperatures show grain comminution (Fig. 9b–d). We performed quantitative analyses of particle size distribution for the wear products on the fault surfaces using these SEM images (see more details in Appendix 2). From Fig. 9e, f, g, we find that increasing temperature promotes the formation of more fine-grained gouge particles with a dominant size less than  $10 \mu\text{m}$  in diameter. This indicates that the gouge particle size may be responsible for the different fault sliding behavior, as observed during the fluid injection tests.

## 5 Discussion

### 5.1 Effect of fluid pressurization rate

Together with the present experimental results, we compiled peak slip velocities caused by varying fluid

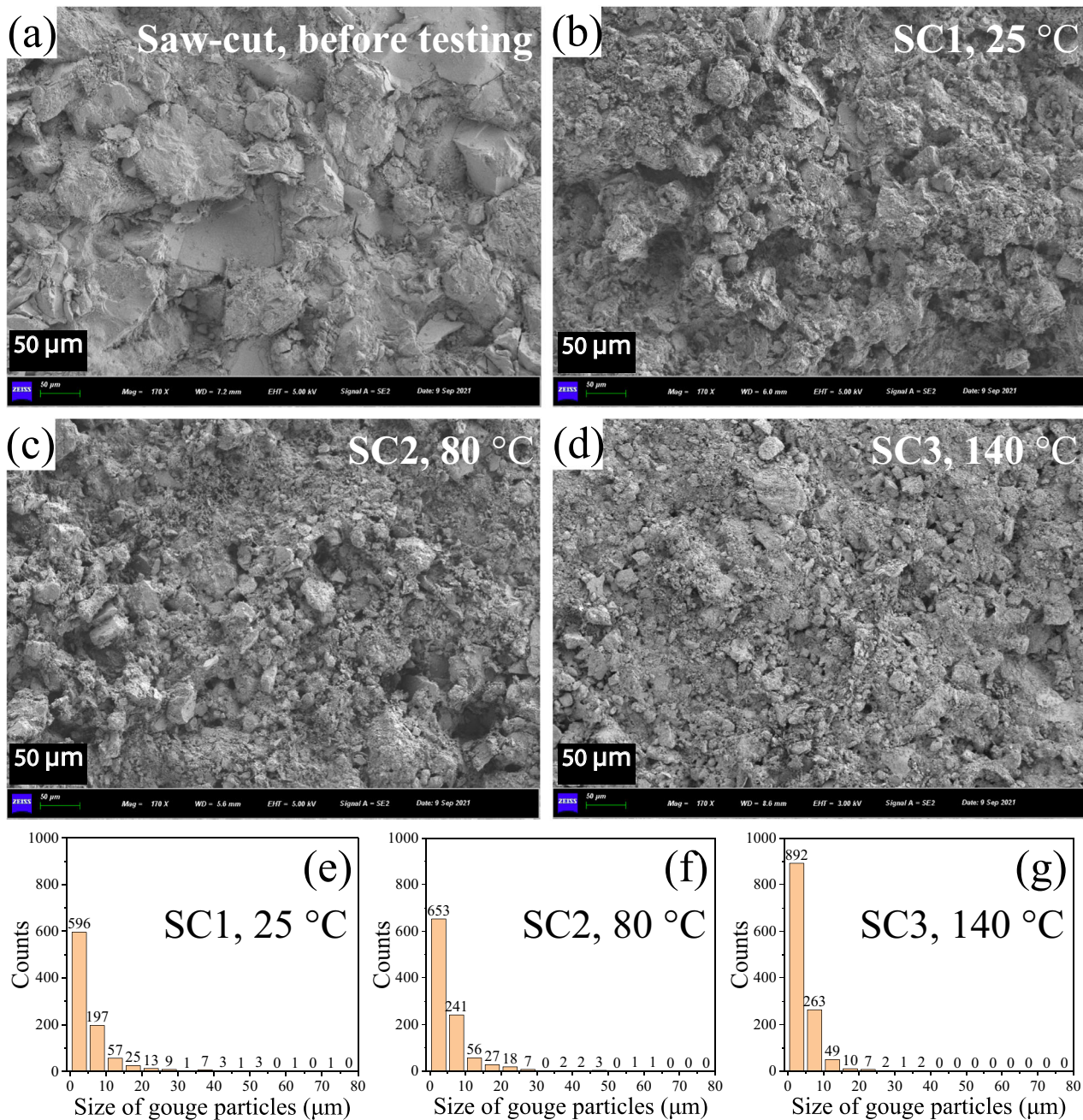


**Fig. 9** Microstructures and gouge particles size distribution for grains on fault surfaces. **a** The initial surfaces of saw-cut sample before the experiments. The post-mortem surface (**b**) and gouge particles size distribution (**e**) of sample SC1 at 25 °C. The post-mortem surface (**c**) and gouge particles size distribution (**f**) of sample SC2 at 80 °C. The post-mortem surface (**d**) and gouge particle size distribution (**g**) of sample SC3 at 140 °C

pressurization rates from the previous experiments under the similar stress relaxation conditions (e.g., [48, 71]). The combined datasets span across four orders of magnitude in fluid pressurization rate, as shown in Fig. 10. It clearly shows that the peak slip velocity caused by fluid injection scales with fluid pressurization rate, for different confining pressures and rock types. At a pressurization rate of 0.5 MPa/min, we recorded a peak slip velocity of around 0.3  $\mu\text{m/s}$ , comparable to the experiments by Wang et al.

[71] on a saw-cut fault in Bentheim sandstone. Multiscale geophysical evidences including the field-scale induced seismicity occurring in Oklahoma caused by wastewater injection [34, 73] and laboratory experiments [48, 71] have suggested that fluid injection rate controls magnitude and stability of induced slip. This is also supported by our experimental observations that peak slip velocities of injection-induced slip events positively scale with pressurization rates.

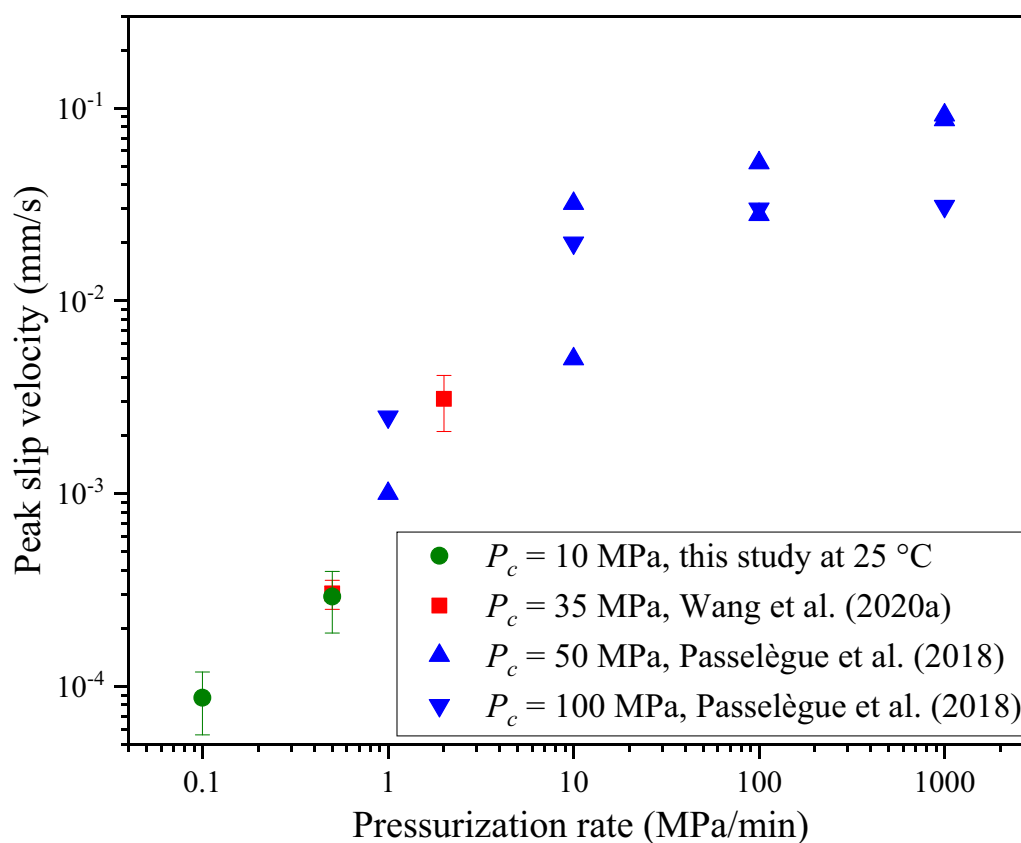


**Fig. 10** Peak slip velocities of induced fault slip as a function of fluid pressurization rate in laboratory injection-induced shear slip experiments at room temperature.  $P_c$  denotes the confining pressure. Note that the mean values of peak slip velocity in this study and in Wang et al. [71] are given with standard deviation

## 5.2 Effect of temperature

The fluid injection experiments were performed at undrained condition, and only about 1.5 mL of water was injected upon the end of the experiments (Figs. 6 and 7). In addition, there was a volume of about 0.4 mL in the thin connection tubes exposed to the heated triaxial chamber. Thus, we expect that the water injected at our low pressurization rates was heated to the ambient temperature before reaching the fault surfaces. This is notably different to the fluid injection experiments performed under drained boundary conditions by Kc and Ghazanfari [31]. In our experiments, faults displayed substantial shear stress relaxation when the position of the axial hydraulic piston was fixed at constant fluid pressures (Figs. 6 and 7). Such observed stress relaxation that was measured globally with an internal load cell may be caused by subcritical cracking [1, 11, 16] and/or pressure solution (mineral solution) [55] at hydrothermal conditions.

In our experiments, we expect that the mechanism of pressure solution is likely to operate, particularly at 140 °C [20]. This is supported by the presence of dissolution pits that were observed on the surface of sample SC5 at 140 °C

after experiments (Fig. 11). Although we did not chemically detect the concentration of elements resolved in the effluent because of our unique experimental configuration (undrained conditions), at the comparable hydrothermal conditions (20 ~ 130 °C), Kc and Ghazanfari [31] experimentally found that increasing temperature resulted in an enhanced mineral dissolution rate, particularly for quartz and feldspar. In addition, the formation of fine-grained gouges at 140 °C facilitates a massive increase in grain surface area (Fig. 9), which may in turn increase the contribution of pressure solution process. We roughly estimated the shear strain rates at varying temperatures using the measured stress relaxation data in the first fluid injection period prior to slip initiation. Given the constant elastic properties of loading machine and rock samples [55], the strain rate is proportional to the stress relaxation rate during a laboratory relaxation test, i.e.,  $\dot{\epsilon} = \dot{\sigma}/G$ , with  $G$  being a combined elastic constant of loading machine and sample [i.e.,  $G \approx 2.2$  GPa in our experiments, as estimated by  $G = K_m \times L$  in which  $K_m = 22$  MPa/mm is the shear stiffness of the loading system (loading machine and rock sample) and  $L = 100$  mm is the sample length]. This results in the estimated strain rate with an order of

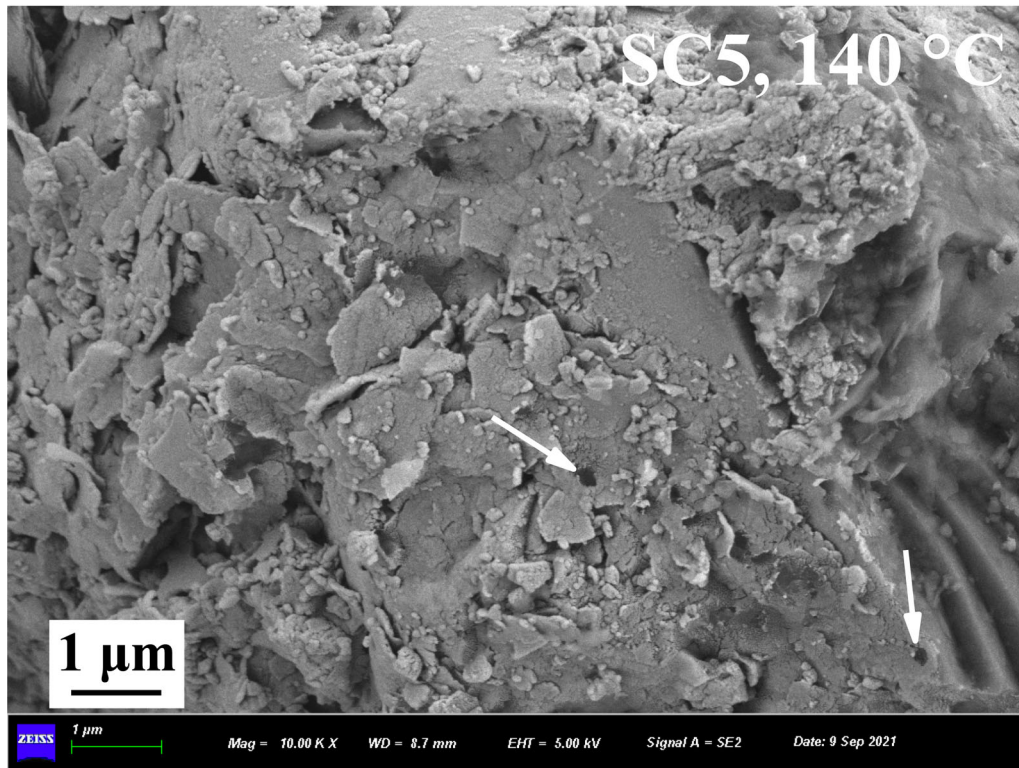


**Fig. 11** Possible dissolution pits on the fault surface after the experiment on Sample SC5 at 140 °C

**Table 3** Summary of shear strain rates estimated from the stress relaxation stages

Samples	SC1	SC2	SC3	SC4	SC5
T (°C)	25	80	140	25	140
Strain rate (s <sup>-1</sup> )	$2.2 \times 10^{-8}$	$3.2 \times 10^{-8}$	$2.7 \times 10^{-8}$	$2.2 \times 10^{-8}$	$5.4 \times 10^{-8}$

magnitude of  $10^{-8} \text{ s}^{-1}$  (see Table 3). Considering that the pressure solution rate may be higher at the locked state of fault [20], the marked sensitivity of strain rate to temperature was clearly observed for samples tested at the pressurization rate of 0.5 MPa/min (i.e., increased by a factor of two from 25 °C to 140 °C). For wet sandstone samples, several studies (e.g., [11, 45, 54, 55]) suggest that deformation rate is controlled by the kinetics of water-assisted stress corrosion at intermediate to high strain rates ( $10^{-7}$  to  $10^{-4} \text{ s}^{-1}$ ), whereas the pressure solution dominates the deformation process at low strain rates ( $10^{-9}$  to  $10^{-8} \text{ s}^{-1}$ ). Considering that subcritical cracking (brittle creep) has been reported to predominantly occur at high stress levels (e.g., beyond yielding stress or dilatancy-dominated stress levels for the intact rock sample, see [27] and [12]), the subcritical cracking mechanism could be less important in our experiments because of the applied low stress levels. Furthermore, previous experiments on the frictional properties of quartz gouge under the hydrothermal conditions revealed that quartz could undergo significant healing due

to solution transfer at a moderate temperature (100 ~ 200 °C) [41]. These observations suggest that pressure solution and associated solution transfer healing mechanisms may be active concurrently in our experiments. The fault can be restrengthened during the shut-in period by either increasing the true area of contact through pressure solution or increasing the quality of contact through healing at hydrothermal conditions. The release of more restored energy from contact asperities may be one reason for the higher slip velocity of induced slip events occurring at an elevated temperature of 140 °C, as observed in our experiments.

### 5.3 Injection-induced slip associated with injected fluid volume

Several models exist that relate the injected fluid volume to cumulative (and maximum) seismic moment and maximum event magnitude [21, 39, 65]. However, the theoretical and laboratory studies of moment–volume relation so

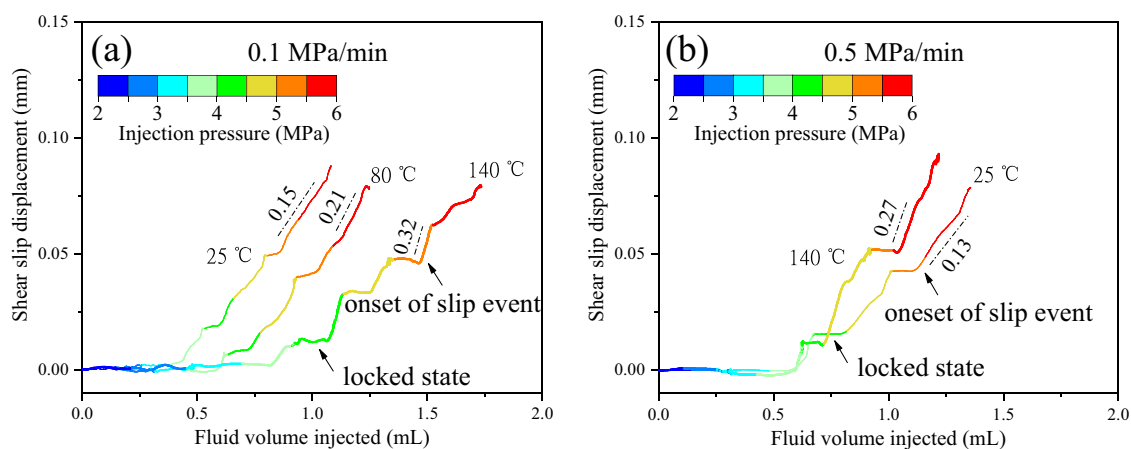


**Fig. 12** **a** The relation between shear slip displacement and fluid volume injected in faults since fluid injection at a pressurization rate of 0.1 MPa/min and at varying temperatures. **b** The relation between shear slip displacement and fluid volume injected in faults since fluid injection at a pressurization rate of 0.5 MPa/min and at varying temperatures. All curves are color-coded by injection pressure. Note that the dashed dot lines and values nearby represent the corresponding slopes after fault reactivation

far do not take the influence of temperature into account. The shear geodetic moment ( $M_0$ ) is defined as the product of shear modulus  $G$ , fault area  $A$ , and average shear slip displacement  $u$  (i.e.,  $M_0 = GAu$ ). Assuming constant shear modulus and finite fault area,  $M_0$  is directly proportional to slip displacement. The results of our study show that the moment (or shear slip displacement)–volume relation is affected by temperature (Fig. 12). Laboratory faults show a delayed onset and a smaller amount of total slip for a given fluid volume injected with increasing temperature at a pressurization rate of 0.1 MPa/min (Fig. 12a). This may be due to the temperature-dependent healing effect at the locked state, and faults need a higher fluid injection energy to be reactivated. After the onset of continued slip by fluid injection, (Fig. 12a), the slope of slip displacement versus fluid-injected volume shows an increasing trend with increasing temperature, (i.e., from 0.15 to 0.32 in Fig. 12a), corresponding to the observed higher velocity of fault slip (Fig. 6a). Such a similar observation also holds for the pressurization rate of 0.5 MPa/min (Fig. 12b).

#### 5.4 Frictional stability of injection-induced slip

Our experiments show that injection-induced fault slip is affected by temperature and fluid pressurization rate on smooth saw-cut faults. Slow fault slip events occur at all experimental conditions. At room temperature of 25 °C, the sample-averaged friction coefficients of faults exhibit strengthening trends in the latter two fluid injection periods, irrespective of pressurization rates. However, this is less clear at elevated temperatures. This indicates that increasing temperature ( $\leq 140$  °C) destabilizes injection-induced fault slip. Microstructure observations of deformed specimens reveal more fine-grained gouge particles as

temperature increases (Fig. 9). This is consistent with experimental results by Bedford and Faulkner [5] who found that fine-grained gouges promote the occurrence of unstable stick–slip behavior. Furthermore, pressure solution promoted by increasing temperature may weaken the frictional stability of faults [44]. To evaluate the stability of fault slip induced by fluid injection at elevated temperatures, we conducted velocity-stepping tests on water-saturated saw-cut sandstone samples. The stability of laboratory fault slip is expected to depend on the comparison between the critical stiffness ( $k_c$ ) that is determined by frictional constitutive parameters ( $a$ ,  $b$ , and  $D_c$ ) and the stiffness of the loading system ( $K_m$ ) [17]. The velocity-stepping tests performed on natural or artificial granular fault gouges indicate that the frictional stability parameters ( $a$ – $b$ ) are affected by effective normal stress and temperature [6, 33, 43, 49, 56]. The measured frictional stability parameters ( $a$ – $b$ ) in our velocity-stepping tests performed on water-saturated saw-cut samples show a gradual reduction with increasing temperature ( $\leq 140$  °C) and confining pressure, in agreement with the previous observations of the velocity-strengthening at room temperature but velocity-weakening from 100 to 350 °C [8, 9] for wet granite at hydrothermal conditions. In the absence of water, a transition from fault creep to slow and fast ruptures was experimentally observed on dry dolostone faults with increasing both confining pressure ( $P_c \leq 100$  MPa) and temperature ( $T \leq 100$  °C) [47]. This is also reflected by the higher peak slip velocities associated with injection-induced fault slip that were observed at 140 °C in our experiments. To estimate fault constitutive parameters, we used similar confining pressures as in the fluid injection tests. For a velocity-weakening fault, unstable slip occurs if the loading system stiffness is less than the critical stiffness

[17, 52]. Using the RSF parameters measured at the boundary conditions of 8 MPa confining pressure and of 140 °C temperature, the critical stiffness ( $k_c$ ) is calculated to be about 1.77 MPa/mm using  $k_c = (P_c - P_p)(b - a)/D_c$  [17, 52]. This value, based on the linear stability analysis, is much less than the loading system stiffness ( $K_m \approx 22$  MPa/mm).

### 5.5 Implications for injection-induced seismicity

In contrast to the conventional injection protocol with monotonic injection of high-pressure fluids, the stepwise injection of fluid pressure we applied in this study allows relaxation of fault stress and promotes deceleration of fault slip. The constant normal stress was maintained during fluid injection into the laboratory faults, suggesting that the effect of poroelastic stressing was neglected in our experiments. The normal and shear stresses acting on the fault plane may be altered during fluid injection and then may stabilize or destabilize the fault, depending on the orientation of faults with respect to the injection well and fault regimes [22, 67]. The mechanism of poroelastic stressing is often used to explain the remotely induced earthquakes that have no hydraulic connection to injection source (e.g., [22]). In contrast, in our experiments, fluid overpressure was directly injected into fracture interfaces, and the fluid pressure equilibrated rapidly across the entire fracture planes, which may correspond to the scenario of induced microseismicity in the fracture system close to the injection source. We experimentally observed the marked dilation of fault zones associated with fluid injection and fault slip, which has also been reported in the in situ fluid injection experiments [24]. The resulting dilation may in turn alter the transport properties of fault zones and then further affect the spatiotemporal distribution of pore pressure and induced seismicity. For less permeable fault zones (i.e., dilatancy occurs more rapidly than fluid pressure diffusion), shear-induced dilation may result in transient fluid pressure decrease within the fault, tending to prohibit further slip (i.e., dilatant hardening) [51]. However, we did not clearly observe such dilatant hardening behavior, possibly due to the high permeability of our laboratory faults.

During the stimulation of geothermal and tight oil/gas reservoirs as well as waste fluid disposal projects [38], the injected fluid may reach the vicinity of natural faults/fractures subjected to elevated temperatures [66, 72]. Our experiments suggest that at a shallow depth ( $P_c \approx 10$  MPa), a high in situ temperature (maximum temperature  $\approx 140$  °C) may promote the instability of injection-induced fault slip. Previous studies on granite and dolostone fault materials show the similar observation that increasing temperature ( $< 200$  °C) may destabilize the

displacement-driven fault slip [8, 47]. Considering that natural faults may be subjected to a higher normal stress with depth, our velocity-stepping tests and other studies (e.g., [5, 25]) imply that the probability of occurrence of earthquakes is likely to increase with depth (normal stress  $< 150$  MPa), consistent with the geophysical observations [46]. It is worthwhile to note that our experiments were performed at isothermal conditions, neglecting the thermal stress induced by the temperature gradient during fluid operations. Indeed, thermal stress may cause fault deformation (slip) and permeability modification, which has been reported in the laboratory experiments (e.g., [4, 31]) and geothermal fields (e.g., [29]). Thus, for a critically stressed fault embedded in a geothermal reservoir, we speculate that high environment temperature and high normal stress may destabilize injection-induced fault slip. In contrast to laboratory-simulated faults, natural faults usually have more complex permeability structures, and the response of natural faults to fluid overpressure involves coupled thermo-hydrological-mechanical processes. The permeability evolution associated with fault slip (e.g., shear-induced dilation/compaction), poroelastic effects, and the interplay between fluid diffusion and aseismic slip under a given injection protocol may jointly alter the fault's seismic/aseismic response (e.g., [7, 13, 23, 24]), but go beyond the scope of the present study.

## 6 Conclusions

In the present study, we investigated injection-induced slip behavior on critically stressed laboratory faults by increasing fluid pressure from 2 to 6 MPa at a constant rate of 0.1 or 0.5 MPa/min under the conditions of a constant confining pressure (10 MPa) and of varying temperatures (i.e., 25, 80, and 140 °C, respectively). Our experimental results indicate that the sliding modes of fractured samples are controlled by temperature at different pressurization rates. Slow fault slip events were observed at all temperature conditions, while several episodes of slip events with a higher slip velocity were induced by fluid pressurization as the temperature increased to 140 °C. The measured RSF parameters suggest that for a relatively high normal stress, increasing temperature tends to destabilize injection-induced fault slip. The microstructural observations show that more fine-grained fault gouge particles have been formed and the effect of pressure solution may play a role at a high temperature. Our experimental results can provide an important implication for injection-induced seismicity that occurs in the geothermal system.

## Appendix 1: Effects of temperature and pressurization rate on fluid pressure distribution

In our experimental configuration, the temporal and spatial variations of fluid pressure ( $P_f$ ) along the intact sandstone sample (50 mm in diameter and 100 mm in length ( $L$ )) can be calculated using the one-dimensional pressure diffusion equation, as expressed by [50]

$$\frac{\partial P_f(x,t)}{\partial t} = D \frac{\partial^2 P_f(x,t)}{\partial x^2} \quad (4)$$

where  $x$  is the distance along the sample from the injection end,  $t$  is the time, and  $D$  is the hydraulic diffusivity.

Then, the relation between hydraulic diffusivity ( $D$ ) and permeability ( $k$ ) can be constrained by [60]

$$D = \frac{k}{\eta\phi(C_f + C_\phi)} \quad (5)$$

where  $\eta$  is the water viscosity ( $\eta_{water} \approx 8.89 \times 10^{-4}$  Pas at 25 °C and  $1.98 \times 10^{-4}$  Pas at 140 °C),  $\phi$  is the porosity ( $\phi \approx 10\%$ ),  $C_f$  is the water compressibility ( $C_f \approx 0.5 \text{ GPa}^{-1}$ ), and  $C_\phi$  is the elastic compressibility of pore space ( $C_\phi \approx 1.0 \text{ GPa}^{-1}$ ). The permeability ( $k$ ) of the intact sample is about  $1.36 \times 10^{-19} \text{ m}^2$  at effective confining pressure of 6 MPa, which results in the rock matrix's hydraulic diffusivity ( $D$ ) of about  $1.02 \times 10^{-6} \text{ m}^2/\text{s}$  at 25 °C and  $4.58 \times 10^{-6} \text{ m}^2/\text{s}$  at 140 °C.

For simplicity, the fluid pressure along the sample constitutes the initial condition:

$$P_f(x,0) = 0, \text{ for } 0 \leq x \leq L \quad (6)$$

In our injection-induced shear slip test, considering that the fluid pressure was increased at a constant rate  $R$  (i.e., 0.1 or 0.5 MPa/min), the temporal evolution of fluid pressure at the injection end (upstream) can be determined by

$$P_f(0,t) = Rt \quad (7)$$

An undrained condition at the monitoring end (downstream) can be described by

$$\partial P_f / \partial x = 0, \text{ at } x = L \quad (8)$$

Under the given boundary conditions above (i.e., Eqs. 6, 7, and 8), we obtain the analytical solution to Eq. (4), as expressed by [50]

$$P_f(x,t) = R_f \frac{2}{L} \sum_{n=0}^{\infty} \sin(\lambda_n x) \frac{(D\lambda_n^2 t - 1) + \exp(-D\lambda_n^2 t)}{D\lambda_n^3}, \quad (9)$$

for  $0 \leq x \leq L$

where  $\lambda_n = \pi(2n + 1)/2L$ .

As shown in Fig. 13, the distribution of fluid pressure along the intact sandstone rock matrix is calculated using Eq. (9) at given times. It indicates that about 900 s is needed for fluid overpressure front to reach the monitoring end, and about  $4 \times 10^5$  s is required to achieve a homogeneous fluid pressure distribution in the rock matrix (Fig. 13). Hence, we believe that the injected fluid volume is constrained in the fault zone during the injection-induced shear slip test.

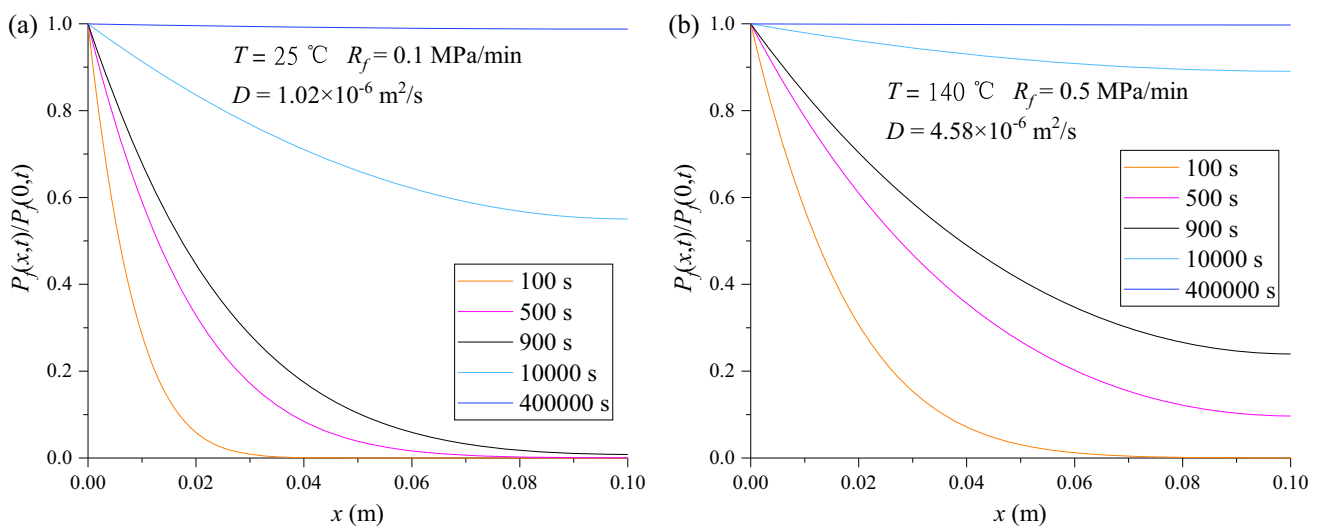


**Fig. 13** Snapshots of fluid pressure distribution along the intact sandstone sample with a length of  $L = 0.1$  m at given times ( $t = 100, 500, 900, 10000$ , and  $400,000$  s, respectively) under two extreme conditions, i.e., **a** the lowest experimental temperature (25 °C) with a pressurization rate of 0.1 MPa/min and **b** the highest experimental temperature (140 °C) with a pressurization rate of 0.5 MPa/min



## Appendix 2: Calculation of gouge particle size distribution

Using the SEM images of post-mortem samples, we calculated the gouge particle size distribution on the worn fault surface through image processing software (ImageJ, <http://imagej.net/Welcome>). Firstly, the raw image was transformed to a format of 8-bit (black-and-white format). Then, the size of image pixel was calibrated by the scale bar on the SEM image. After that, gouge particles were highlighted by selecting a suitable contrast threshold. To avoid identifying individual pixels as gouge particles, an area threshold of  $5 \mu\text{m}^2$  was set to filter out disturbing information. Finally, we obtained the statistical results of area information of gouge particles. To explicitly compare the particle size distribution, the final data were converted to the equivalent circular area with an equivalent diameter.

**Acknowledgments** The authors are grateful to Georg Dresen for providing constructive suggestion and comments on the first version of our manuscript. This study was jointly supported by the National Key R&D Program of China (Grant No. 2019YFE0100100) and the National Natural Science Foundation of China (Grant No. 41972316). LW is grateful to the Open Research Fund of State Key Laboratory of Geomechanics and Geotechnical Engineering, Institute of Rock and Soil Mechanics, Chinese Academy of Sciences (Grant No. SKLGME021003). We thank two anonymous reviewers and the Editor Ronaldo I. Borja for providing constructive comments and suggestions that have substantially improved the present work.

**Funding** Open Access funding enabled and organized by Projekt DEAL. This study was funded by Key Technology Research and Development Program of Shandong, 2019YFE0100100, Xiaochun Li; Innovative Research Group Project of the National Natural Science Foundation of China, 41972316, Xiaochun Li; and Open Research Fund of State Key Laboratory of Geomechanics and Geotechnical Engineering, Institute of Rock and Soil Mechanics, Chinese Academy of Sciences, SKLGME021003, Lei Wang.

## Declarations

**Conflict of interest** The authors declare that they have no conflict of interest.

**Open Access** This article is licensed under a Creative Commons Attribution 4.0 International License, which permits use, sharing, adaptation, distribution and reproduction in any medium or format, as long as you give appropriate credit to the original author(s) and the source, provide a link to the Creative Commons licence, and indicate if changes were made. The images or other third party material in this article are included in the article's Creative Commons licence, unless indicated otherwise in a credit line to the material. If material is not included in the article's Creative Commons licence and your intended use is not permitted by statutory regulation or exceeds the permitted use, you will need to obtain permission directly from the copyright holder. To view a copy of this licence, visit <http://creativecommons.org/licenses/by/4.0/>.

## References

- Atkinson BK (1984) Subcritical crack growth in geological materials. *J Geophys Res Solid Earth* 89:4077–4114. <https://doi.org/10.1029/JB089iB06p04077>
- Atkinson GM, Eaton DW, Igonin N (2020) Developments in understanding seismicity triggered by hydraulic fracturing. *Nat Rev Earth Environ* 1:264–277. <https://doi.org/10.1038/s43017-020-0049-7>
- Barton N (1973) Review of a new shear-strength criterion for rock joints. *Eng Geol* 7:287–332. [https://doi.org/10.1016/0013-7952\(73\)90013-6](https://doi.org/10.1016/0013-7952(73)90013-6)
- Bauer SJ, Huang K, Chen Q, Ghassemi A, Barrow P (2016) Experimental and numerical investigation of hydro-thermally induced shear stimulation. In: 50th US rock mechanics / geomechanics symposium 2016, pp 8–17
- Bedford JD, Faulkner DR (2021) The role of grain size and effective normal stress on localization and the frictional stability of simulated quartz gouge. *Geophys Res Lett* 48:e2020GL092023. <https://doi.org/10.1029/2020GL092023>
- Bedford JD, Faulkner DR, Allen MJ, Hirose T (2021) The stabilizing effect of high pore-fluid pressure along subduction megathrust faults: evidence from friction experiments on accretionary sediments from the Nankai Trough. *Earth Planet Sci Lett* 574:117161. <https://doi.org/10.1016/j.epsl.2021.117161>
- Bhattacharya P, Viesca RC (2019) Fluid-induced aseismic fault slip outpaces pore-fluid migration. *Science* 364:464–468. <https://doi.org/10.1126/science.aaw7354>
- Blanpied ML, Lockner DA, Byerlee JD (1991) Fault stability inferred from granite sliding experiments at hydrothermal conditions. *Geophys Res Lett* 18:609–612. <https://doi.org/10.1029/91GL00469>
- Blanpied ML, Lockner DA, Byerlee JD (1995) Frictional slip of granite at hydrothermal conditions. *J Geophys Res Solid Earth* 100:13045–13064. <https://doi.org/10.1029/95JB00862>
- Brace WF, Byerlee JD (1970) California earthquakes: why only shallow focus? *Science* 168:1573–1575. <https://doi.org/10.1126/science.168.3939.1573>
- Brantut N, Baud P, Heap MJ, Meredith PG (2012) Micromechanics of brittle creep in rocks. *J Geophys Res Solid Earth*. <https://doi.org/10.1029/2012JB009299>
- Brantut N, Heap MJ, Meredith PG, Baud P (2013) Time-dependent cracking and brittle creep in crustal rocks: a review. *J Struct Geol* 52:17–43. <https://doi.org/10.1016/j.jsg.2013.03.007>
- Cappa F, Guglielmi Y, Nussbaum C, Birkholzer J (2018) On the relationship between fault permeability increases, induced stress perturbation, and the growth of aseismic slip during fluid injection. *Geophys Res Lett* 45:11012–11020. <https://doi.org/10.1029/2018GL080233>
- Cebry SBL, Ke C-Y, McLaskey GC (2022) The role of background stress state in fluid-induced aseismic slip and dynamic rupture on a 3-m laboratory fault. *J Geophys Res Solid Earth* 127:e2022JB024371. <https://doi.org/10.1029/2022JB024371>
- Chester FM (1994) Effects of temperature on friction: constitutive equations and experiments with quartz gouge. *J Geophys Res Solid Earth* 99:7247–7261. <https://doi.org/10.1029/93JB03110>
- Dabloul R, Jin BC, Jha B (2023) Failure analysis of the edge-notched beam test on fluid-exposed Berea Sandstone. *Acta Geotech* 18:4035–4053. <https://doi.org/10.1007/s11440-023-01843-2>
- Dieterich JH (1979) Modeling of rock friction: 1. Experimental results and constitutive equations. *J Geophys Res* 84:2161–2168. <https://doi.org/10.1029/JB084iB05p02161>
- Ellsworth WL (2013) Injection-induced earthquakes. *Science* 341:1225942. <https://doi.org/10.1126/science.1225942>

19. French ME, Zhu W, Banker J (2016) Fault slip controlled by stress path and fluid pressurization rate. *Geophys Res Lett* 43:4330–4339. <https://doi.org/10.1002/2016GL068893>
20. Fu B, Diao Y, Espinosa-Marzal RM (2021) Nanoscale insight into the relation between pressure solution of calcite and interfacial friction. *J Colloid Interface Sci* 601:254–264. <https://doi.org/10.1016/j.jcis.2021.04.145>
21. Galis M, Ampuero JP, Mai PM, Cappa F (2017) Induced seismicity provides insight into why earthquake ruptures stop. *Sci Adv* 3:eaap7528. <https://doi.org/10.1126/sciadv.aap7528>
22. Goebel THW, Brodsky EE (2018) The spatial footprint of injection wells in a global compilation of induced earthquake sequences. *Science* 361:899–904. <https://doi.org/10.1126/science.aat5449>
23. Goebel THW, Weingarten M, Chen X, Haffener J, Brodsky EE (2017) The 2016 Mw5.1 fairview, Oklahoma earthquakes: evidence for long-range poroelastic triggering at >40 km from fluid disposal wells. *Earth Planet Sci Lett* 472:50–61. <https://doi.org/10.1016/j.epsl.2017.05.011>
24. Guglielmi Y, Cappa F, Avouac JP, Henry P, Elsworth D (2015) Seismicity triggered by fluid injection-induced aseismic slip. *Science* 348:1224–1226. <https://doi.org/10.1126/science.aab0476>
25. Harbord CWA, Nielsen SB, De Paola N, Holdsworth RE (2017) Earthquake nucleation on rough faults. *Geology* 45:931–934. <https://doi.org/10.1130/G39181.1>
26. Healy J, Rubey W, Griggs D, Raleigh C (1968) The denver earthquakes. *Science* 161:1301–1310. <https://doi.org/10.1126/science.161.3848.1301>
27. Heap MJ, Baud P, Meredith PG, Bell AF, Main IG (2009) Time-dependent brittle creep in Darley Dale sandstone. *J Geophys Res Solid Earth*. <https://doi.org/10.1029/2008JB006212>
28. Huang K, Cheng Q, Ghassemi A, Bauer S (2019) Investigation of shear slip in hot fractured rock. *Int J Rock Mech Min Sci* 120:68–81. <https://doi.org/10.1016/j.ijrmm.2019.05.006>
29. Im K, Avouac J-P (2021) On the role of thermal stress and fluid pressure in triggering seismic and aseismic faulting at the Brawley geothermal field. *California Geothermics* 97:102238. <https://doi.org/10.1016/j.geothermics.2021.102238>
30. Ji Y, Hofmann H, Rutter EH, Zang A (2022) Transition from slow to fast injection-induced slip of an experimental fault in granite promoted by elevated temperature. *Geophys Res Lett* 49:e2022GL101212. <https://doi.org/10.1029/2022GL101212>
31. Kc B, Ghazanfari E (2021) Geothermal reservoir stimulation through hydro-shearing: an experimental study under conditions close to enhanced geothermal systems. *Geothermics* 96:102200. <https://doi.org/10.1016/j.geothermics.2021.102200>
32. Kim KH, Ree JH, Kim Y, Kim S, Kang SY, Seo W (2018) Assessing whether the 2017 Mw 5.4 Pohang earthquake in South Korea was an induced event. *Science* 360:1007–1009. <https://doi.org/10.1126/science.aat6081>
33. King DSH, Marone C (2012) Frictional properties of olivine at high temperature with applications to the strength and dynamics of the oceanic lithosphere. *J Geophys Res Solid Earth*. <https://doi.org/10.1029/2012JB009511>
34. Langenbruch C, Zoback AMD (2016) How will induced seismicity in Oklahoma respond to decreased saltwater injection rates? *Sci Adv*. <https://doi.org/10.1126/sciadv.1601542>
35. Lockner DA, Byerlee JD (1994) Dilatancy in hydraulically isolated faults and the suppression of instability. *Geophys Res Lett* 21:2353–2356. <https://doi.org/10.1029/94GL02366>
36. Lockner DA, Summers R, Byerlee JD (1986) Effects of temperature and sliding rate on frictional strength of granite. *Pure Appl Geophys* 124:445–469. <https://doi.org/10.1007/BF00877211>
37. Manjunath GL, Akono AT, Haljasmaa I, Jha B (2023) Role of CO<sub>2</sub> in geomechanical alteration of morrow sandstone across micro–meso scales. *Int J Rock Mech Min Sci* 163:105311. <https://doi.org/10.1016/j.ijrmm.2022.105311>
38. Manjunath GL, Liu Z, Jha B (2023) Multi-stage hydraulic fracture monitoring at the lab scale. *Eng Fract Mech* 289:109448. <https://doi.org/10.1016/j.engfracmech.2023.109448>
39. McGarr A (2014) Maximum magnitude earthquakes induced by fluid injection. *J Geophys Res Solid Earth* 119:1008–1019. <https://doi.org/10.1002/2013JB010597>
40. Meehan CL, Talebi M (2017) A method for correcting field strain measurements to account for temperature effects. *Geotext Geomembr* 45:250–260. <https://doi.org/10.1016/j.geotextmem.2017.02.005>
41. Nakatani M, Scholz CH (2004) Frictional healing of quartz gouge under hydrothermal conditions: 1. Experimental evidence for solution transfer healing mechanism. *J Geophys Res Solid Earth*. <https://doi.org/10.1029/2001JB001522>
42. Nemoto K, Moriya H, Niitsuma H, Tsuchiya N (2008) Mechanical and hydraulic coupling of injection-induced slip along pre-existing fractures. *Geothermics* 37:157–172. <https://doi.org/10.1016/j.geothermics.2007.11.001>
43. Niemeijer AR, Collettini C (2014) Frictional properties of a low-angle normal fault under in situ conditions: thermally-activated velocity weakening. *Pure Appl Geophys* 171:2641–2664. <https://doi.org/10.1007/s00024-013-0759-6>
44. Niemeijer AR, Spiers CJ (2007) A microphysical model for strong velocity weakening in phyllosilicate-bearing fault gouges. *J Geophys Res Solid Earth*. <https://doi.org/10.1029/2007JB005008>
45. Oncken O, Angiboust S, Dresen G (2021) Slow slip in subduction zones: reconciling deformation fabrics with instrumental observations and laboratory results. *Geosphere* 18:104–129. <https://doi.org/10.1130/GES02382.1>
46. Passelègue FX, Almakari M, Dublanchet P, Barras F, Fortin J, Violay M (2020) Initial effective stress controls the nature of earthquakes. *Nat Commun* 11:5132. <https://doi.org/10.1038/s41467-020-18937-0>
47. Passelègue FX, Aubry J, Nicolas A, Fondriest M, Deldicque D, Schubnel A, Di Toro G (2019) From fault creep to slow and fast earthquakes in carbonates. *Geology* 47:744–748. <https://doi.org/10.1130/G45868.1>
48. Passelègue FX, Brantut N, Mitchell TM (2018) Fault reactivation by fluid injection: controls from stress state and injection rate. *Geophys Res Lett* 45:12837–12846. <https://doi.org/10.1029/2018gl080470>
49. Plummakers AMH, Samuelson JE, Niemeijer AR, Spiers CJ (2014) Effects of temperature and CO<sub>2</sub> on the frictional behavior of simulated anhydrite fault rock. *J Geophys Res Solid Earth* 119:8728–8747. <https://doi.org/10.1002/2014JB011575>
50. Polyanin AD (2002) Linear partial differential equations for engineers and scientists. Chapman and Hall/CRC, Boca Raton
51. Rudnicki JW, Chen C-H (1988) Stabilization of rapid frictional slip on a weakening fault by dilatant hardening. *J Geophys Res Solid Earth* 93:4745–4757. <https://doi.org/10.1029/JB093iB05p04745>
52. Ruina A (1983) Slip instability and state variable friction laws. *J Geophys Res* 88:10359–10370. <https://doi.org/10.1029/JB088iB12p10359>
53. Rutter E, Hackston A (2017) On the effective stress law for rock-on-rock frictional sliding, and fault slip triggered by means of fluid injection. *Philos Trans Royal Soc A Math Phys Eng Sci*. <https://doi.org/10.1098/rsta.2016.0001>
54. Rutter EH (1983) Pressure solution in nature, theory and experiment. *J Geol Soc* 140:725–740. <https://doi.org/10.1144/gsjgs.140.5.0725>

55. Rutter EH, Mainprice DH (1978) The effect of water on stress relaxation of faulted and unfaulted sandstone. *Pure Appl Geophys* 116:634–654. <https://doi.org/10.1007/BF00876530>
56. Sawai M, Niemeijer AR, Plümpner O, Hirose T, Spiers CJ (2016) Nucleation of frictional instability caused by fluid pressurization in subducted blueschist. *Geophys Res Lett* 43:2543–2551. <https://doi.org/10.1002/2015GL067569>
57. Schultz R, Skoumal RJ, Brudzinski MR, Eaton D, Baptie B, Ellsworth W (2020) Hydraulic fracturing-induced seismicity. *Rev Geophys* 58:e2019RG000695. <https://doi.org/10.1029/2019RG000695>
58. Scuderi MM, Collettini C (2018) Fluid injection and the mechanics of frictional stability of shale-bearing faults. *J Geophys Res Solid Earth* 123:8364–8384. <https://doi.org/10.1029/2018jb016084>
59. Scuderi MM, Collettini C, Marone C (2017) Frictional stability and earthquake triggering during fluid pressure stimulation of an experimental fault. *Earth Planet Sci Lett* 477:84–96. <https://doi.org/10.1016/j.epsl.2017.08.009>
60. Segall P, Rice JR (1995) Dilatancy, compaction, and slip instability of a fluid-infiltrated fault. *J Geophys Res Solid Earth* 100:22155–22171. <https://doi.org/10.1029/95JB02403>
61. Shen N, Li X, Zhang Q, Wang L (2021) Comparison of shear-induced gas transmissivity of tensile fractures in sandstone and shale under varying effective normal stresses. *J Nat Gas Sci Eng* 95:104218. <https://doi.org/10.1016/j.jngse.2021.104218>
62. Shen N, Wang L, Li X (2022) Laboratory simulation of injection-induced shear slip on saw-cut sandstone fractures under different boundary conditions. *Rock Mech Rock Eng* 55:751–771. <https://doi.org/10.1007/s00603-021-02689-4>
63. Skarbak RM, Savage HM (2019) RSFit3000: a Matlab GUI-based program for determining rate and state frictional parameters from experimental data. *Geosphere* 15:1665–1676. <https://doi.org/10.1130/ges02122.1>
64. Stesky RM (1978) Rock friction-effect of confining pressure, temperature, and pore pressure. *Pure Appl Geophys* 116:690–704. <https://doi.org/10.1007/BF00876532>
65. van der Elst NJ, Page MT, Weiser DA, Goebel THW, Hosseini SM (2016) Induced earthquake magnitudes are as large as (statistically) expected. *J Geophys Res Solid Earth* 121:4575–4590. <https://doi.org/10.1002/2016JB012818>
66. Vilarrasa V, Carrera J, Olivella S, Rutqvist J, Laloui L (2019) Induced seismicity in geologic carbon storage. *Solid Earth* 10:871–892. <https://doi.org/10.5194/se-10-871-2019>
67. Wang L, Bai B, Li X, Liu M, Wu H, Hu S (2016) An analytical model for assessing stability of pre-existing faults in Caprock caused by fluid injection and extraction in a reservoir. *Rock Mech Rock Eng* 49:2845–2863. <https://doi.org/10.1007/s00603-016-0933-0>
68. Wang L, Kwiatek G, Bohnhoff M, Rybacki E, Dresen G (2024) Injection-induced fault slip and associated seismicity in the lab: insights from source mechanisms, local stress states and fault geometry. *Earth Planet Sci Lett* 626:118515. <https://doi.org/10.1016/j.epsl.2023.118515>
69. Wang L et al. (2024) Fault roughness controls injection-induced seismicity. In: *Proceedings of the national academy of sciences*, 121:e2310039121. Doi: <https://doi.org/10.1073/pnas.2310039121>
70. Wang L, Kwiatek G, Rybacki E, Bohnhoff M, Dresen G (2020) Injection-induced seismic moment release and laboratory fault slip: implications for fluid-induced seismicity. *Geophys Res Lett* 47:e2020GL089576. <https://doi.org/10.1029/2020GL089576>
71. Wang L, Kwiatek G, Rybacki E, Bonnelye A, Bohnhoff M, Dresen G (2020) Laboratory study on fluid-induced fault slip behaviour: the role of fluid pressurization rate. *Geophys Res Lett* 47:e2019GL086627. <https://doi.org/10.1029/2019GL086627>
72. Wanniarachchi WAM, Ranjith PG, Perera MSA (2017) Shale gas fracturing using foam-based fracturing fluid: a review. *Environ Earth Sci* 76:91. <https://doi.org/10.1007/s12665-017-6399-x>
73. Weingarten M, Ge S, Godt JW, Bekins BA, Rubinstein JL (2015) High-rate injection is associated with the increase in U.S. mid-continent seismicity. *Science* 348:1336–1340. <https://doi.org/10.1126/science.aab1345>
74. Ki Y (2013) An attempt to correct strain data measured with vault-housed extensometers under variations in temperature. *Tectonophysics* 599:89–96. <https://doi.org/10.1016/j.tecto.2013.04.001>
75. Ye Z, Ghassemi A (2018) Injection-induced shear slip and permeability enhancement in granite fractures. *J Geophys Res Solid Earth* 123:9009–9032. <https://doi.org/10.1029/2018JB016045>
76. Ye Z, Ghassemi A (2020) Heterogeneous fracture slip and aseismic-seismic transition in a Triaxial injection test. *Geophys Res Lett* 47:87739. <https://doi.org/10.1029/2020gl087739>
77. Zhang Q, Li X, Bai B, Pei L, Shi L, Wang Y (2019) Development of a direct-shear apparatus coupling with high pore pressure and elevated temperatures. *Rock Mech Rock Eng* 52:3475–3484. <https://doi.org/10.1007/s00603-019-1735-y>

**Publisher's Note** Springer Nature remains neutral with regard to jurisdictional claims in published maps and institutional affiliations.